CHEMISTRY OF MATERIALS

pubs.acs.org/cm

Article

First-Principles and Experimental Investigation of ABO_4 Zircons as Calcium Intercalation Cathodes

Jiyoon Kim, Dogancan Sari, Qian Chen, Ann Rutt, Gerbrand Ceder, and Kristin A. Persson*

Cite This: https://doi.org/10.1021/acs.chemmater.4c00062

Read Online

ACCESS | Metrics & More | Article Recommendations | Supporting Information

ABSTRACT: Identifying next-generation batteries with multivalent ions, such as Ca^{2+} is an active area of research to meet the increasing demand for large-scale, renewable energy storage solutions. Despite the promise of higher energy densities with multivalent batteries, one of their main challenges is addressing the sluggish kinetics in cathodes that arise from stronger electrostatic interactions between the multivalent ion and host lattice. In this paper, zircons are theoretically and experimentally evaluated as Ca cathodes. A migration barrier as low as 113 meV is computationally found in YVO_4, which is the lowest Ca^{2+} barrier reported to date. Low barriers are confirmed across 18 zircon compositions, which are related to the low coordination change and reduced interstitial site preference of Ca^{2+} along the diffusion pathway. Among the four materials ($BiVO_4$, YVO_4, $EuCrO_4$, and $YCrO_4$) that were synthesized, characterized, and electrochemically cycled, the highest initial capacity of 81 mA h/g and the most reversible capacity of 65 mA h/g were achieved in YVO_4 and $BiVO_4$, respectively. Despite the facile migration of multivalent ions in zircons, density functional theory predictions of the unstable, discharged structures at higher Ca^{2+} concentrations ($Ca_{x>0.25}ABO_4$), the low dimensionality of the migration pathway, and the defect analysis of the B site atom can rationalize the limited intercalation observed upon electrochemical cycling.

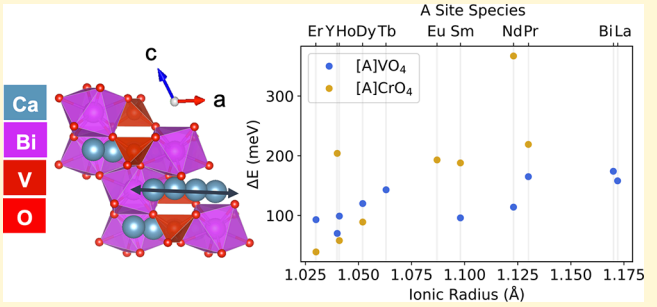

INTRODUCTION

There is a growing interest in next-generation batteries with multivalent ions to meet large-scale energy storage demands.[1−3] Among these candidates, Ca-ion batteries offer several advantages: Ca^{2+} is a low cost and nontoxic alkaline element; it is the fifth most abundant mineral in the earth's crust; and its standard reduction potential is closest to that of Li^+ compared to other alternatives such as Na^+, K^+, and Mg^{2+} (−2.87 V vs SHE for Ca^{2+} vs −3.04 V vs SHE for Li^+), which may allow for higher operating voltages as well as energy densities.[4,5] Reversible cycling in Ca-ion batteries has recently been demonstrated in a few candidates, albeit with significant cell polarization and capacity fade. The NASICON-structured $NaV_2(PO_4)_3$ delivers a capacity of 70 mA h/g at 3.2 V for 30 cycles at room temperature after an activation process at 75 °C.[6,7] Also, $Na_{0.5}VPO_{4.8}F_{0.7}$ (NVPF) can achieve 75 mA h/g at 75 °C, retaining over 90% of its capacity after 500 cycles and 63% after 50 cycles in a full cell configuration.[8] Despite recent advances in Ca cathode research, discovering high-voltage and energy-dense Ca cathode materials that retain capacity with repeated cycling at room temperature remains challenging.

Prior work has been done to screen for promising Ca cathode candidates with density functional theory (DFT) among layered, perovskite, spinel, as well as ternary oxide and chalcogenide materials,[9−12] but the search space has either been limited to families of structurally similar materials, compounds that already contain Ca^{2+}, and/or substitutions of other working ions with Ca^{2+}. An automated workflow to discover Mg intercalation electrodes has been reported and offers inspiration for cathode screening efforts with other working ions; however, it solely evaluates discharged materials where the working ion is already present and its crystallographic sites are known.[13] Notably, the most successful Ca cathodes were originally synthesized without Ca^{2+}: e.g., the previously discussed NASICON and NVPF Ca cathodes were synthesized as $Na_3V_2(PO_4)_3$ and $Na_{1.5}VPO_{4.8}F_{0.7}$, respectively, and then partially desodiated electrochemically to obtain $NaV_2(PO_4)_3$ and $Na_{0.5}VPO_{4.8}F_{0.7}$.[6−8] As a counter example, CaV_2O_4 was synthesized in the discharged state and the reversibility of its redox mechanisms was demonstrated; however, limited cycle life data were reported, and concerns over electrolyte degradation were noted.[14] The strong correlation between successful cycling of multivalent cathodes and their charged, or "empty host" native state, is rationalized by previously elucidated design rules for multivalent-ion diffusion.[15] Specifically, multivalent ions in oxides and

Received: January 8, 2024
Revised: April 9, 2024
Accepted: April 10, 2024

chalcogenides are usually found in deep potential wells, originating from the dual charge, as well as their strong preference for certain coordination sites. Hence, it seems plausible to assume that successful cathodes will be found among the large chemical space of materials where the ion is not already present in the lattice. This has led us to an examination of possible Ca cathodes among materials that do not contain Ca^{2+} a priori and have unknown intercalation sites.

There are several publications on zircon compounds reported in the literature,[16−19] but there are limited studies on their transport properties and electrochemical behavior.[20−22] The zircon family has recently been explored as potential Mg cathodes.[23] Remarkable Mg-ion mobility was found to be related to the low coordination change in Mg^{2+} along the migration pathway. This family of tetragonal materials (space group $I4_1/amd$) with the ABO_4 zircon-type structure spans a large chemical space and consists of alternating edge-sharing AO_8 dodecahedra alongside BO_4 tetrahedra that form one-dimensional channels.[24] In this work, metastable Ca^{2+} intercalation sites and percolating migration pathways were identified in the zircon channels (Figure 1) using an insertion algorithm[25] and graph-based

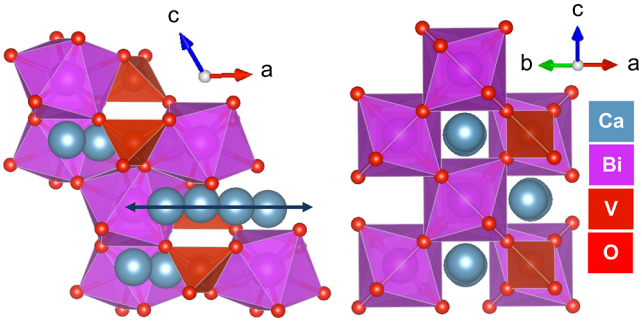

Figure 1. Ca^{2+} intercalation sites in $BiVO_4$ spaced 1.6 Å apart from their neighboring Ca^{2+} interstitial atoms. The blue arrow indicates the direction of Ca diffusion in the identified linear migration pathway.

migration analysis[26] developed by Shen et al. These linear migration pathways for Ca^{2+} consisting of 1.6 Å characteristic hops are consistent with the interstitial sites previously reported in magnesiated and unmagnesiated zircons.[23,24] In this work, 18 ABO_4 zircon materials are theoretically evaluated as potential Ca cathode candidates (A = [Bi, Dy, Er, Eu, Ho, La, Nd, Pr, Sm, Tb, Y], B = [Cr, V]). Remarkably low Ca^{2+} migration barriers in the defect-free structures are confirmed across all compositions, with the lowest barrier being 113 meV in YVO_4. These cathodes are thermodynamically stable in their discharged state at low concentrations of Ca^{2+}, which may limit intercalation and therefore capacity. Subsequent experimental synthesis, characterization, and electrochemical evaluation were conducted on a subset consisting of $BiVO_4$, YVO_4, $EuCrO_4$, and $YCrO_4$. The largest specific capacity of 81 mA h/g and the most reversible capacity of 65 mA h/g were achieved with YVO_4 and $BiVO_4$, respectively. The limited Ca^{2+} intercalation and capacity loss are attributed to the instability of the discharged cathodes at higher Ca concentrations and the undesirable coordination environment of the transition state metal upon reduction.

METHODS

Zircon Ca Cathode Screening Methodology. A screening study of the zircon structure for possible Ca cathode applications was adapted from a method originally developed for Mg battery materials.[27] Possible Ca zircon cathodes were evaluated on a range of criteria of increasing computational cost, including their chemistry, stability, electrode properties, as well as ion mobility. 36 ABO_4 zircon materials without Ca^{2+} and free of radioactive elements were identified in the 2022 version of the Materials Project[28] database using default structure matching criteria as implemented in pymatgen[29] to a known zircon compound YVO_4. The intercalation sites were identified in 30 candidates found in the Inorganic Crystal Structure Database (ICSD) using an insertion algorithm, where Ca^{2+} was inserted in sites with local electronic charge density minima.[25] The most stable DFT-relaxed structure with topotactic insertion, in which the host material does not undergo significant structural changes upon calciation, was selected. If a topotactic insertion structure did not exist, then the candidate was discarded. Ca cathode candidates with an energy above the hull less than 0.2 eV/atom in the discharged state to ensure reasonable expectation of synthesizability,[30,31] an intercalation voltage within the experimentally accessible voltage range of 0.5−4 V, and a volume change upon intercalation (for $Ca_{0.5}ABO_4$) less than 20% were prioritized for ion mobility calculations. With the identified intercalation sites, a periodic graph known as a "migration graph" was populated with symmetrically equivalent sites to locate percolating migration pathways between metastable Ca^{2+} sites in candidate materials.[26] A more robust and less costly alternative to nudged elastic band (NEB) known as ApproxNEB[32] was performed on the remaining 21 zircons to evaluate their migration barriers for Ca^{2+} in the dilute lattice limit. The calculated energy barriers were mapped back onto their respective migration graphs to find the lowest energy pathway for each material according to Dijkstra's algorithm.[26] Candidates without complete ApproxNEB data and pseudopotentials that were unreliable at the time (e.g., Yb) were deprioritized, which led to the 18 zircon materials in this investigation.

DFT Calculations for Electrode Properties. DFT calculations were performed with the Perdew−Burke−Ernzerhof (PBE) generalized-gradient approximation (GGA)[33] and the projector augmented wave approach[34] to approximate the exchange correlation functional as implemented in the Vienna Ab initio Software Package (VASP).[35] "MPRelaxSet" from pymatgen[29] was referenced to apply Hubbard U corrections of U_{Cr} = 3.7 eV and U_V = 3.25 eV, as well as to select pseudopotentials for DFT. A plane-wave cutoff of 520 eV, Monkhorst−Pack k-point mesh density of 64 $Å^{-3}$, total energy convergence criteria of 5×10^{-5} eV, and a force threshold of 5×10^{-2} eV/Å were set for these calculations. DFT relaxations for the insertion site finding step were carried out with these parameters using a python-based workflow implemented in Atomate.[36]

Evaluating Ion Mobility. ApproxNEB calculations were performed on all 18 zircon materials, using the material's charge density to initialize the minimum energy pathway.[32] The image structures were evaluated as single point calculations using a workflow in Atomate.[36] NEB calculations were completed for $EuCrO_4$, $YCrO_4$, $BiVO_4$, and YVO_4 with Transition State Tools for VASP.[37] Both types of calculations were carried out without Hubbard U corrections since GGA + U does not conclusively perform better than GGA in NEB[11,38,39] and assumed to be the case for ApproxNEB as well. The migration barriers were calculated in the dilute lattice limit with a single Ca^{2+} in each supercell structure. Supercell structures with lattice parameters greater than 10 Å (16−32 ABO_4 formula units with 97−193 atoms including Ca^{2+}) were generated with pymatgen[29] to avoid fictitious self-interactions between nearby Ca^{2+} as a result of periodic boundary conditions. These DFT calculations were performed with PBE GGA[33] and the projector augmented wave approach[34] to approximate the exchange correlation functional as implemented in VASP.[35] "MPRelaxSet" from pymatgen[29] was slightly modified to use Gaussian smearing, to assume $\Psi_k = \Psi_{-k}^*$ without symmetry, and to perform a minimum of four electronic self-consistency steps. A plane-

https://doi.org/10.1021/acs.chemmater.4c00062
Chem. Mater. XXXX, XXX, XXX−XXX

Table 1. Theoretical Comparison of $[Mg,Ca]_xABO_4$ (x = [0.5, 1], A = [Y, Eu], and B = [Cr, V]) Zircon Intercalation Electrode Properties Based on DFT Calculations[a]

	zircon Mg cathodes			zircon Ca cathodes		
	$Mg_{0.5}YCrO_4$	$MgEuCrO_4$	$MgYVO_4$	$Ca_{0.5}YCrO_4$	$CaEuCrO_4$	$CaYVO_4$
voltage (V vs Mg/Mg^{2+} or Ca/Ca^{2+})	1.9	1.8	1.0	2.0	2.2	1.1
gravimetric capacity (mA h/g)	131	200	263	119	174	220
migration barrier (meV)	121	107	71	150	193*	113
volume change (%)	6	10	12	13	24	24

[a]The migration barriers were derived from the NEB method (*refers to the provided ApproxNEB barrier for Ca_xEuCrO_4 due to the unavailability of NEB results). Adapted in part with permission from Rutt et al.[23] Copyright 2023, American Chemical Society.

wave cutoff of 520 eV was set. For DFT-ApproxNEB relaxations, the host, end point, and image structure energies were converged to 5×10^{-4} eV with a force tolerance of 5×10^{-2} eV/Å. For DFT-NEB relaxations, the end point structure energies were converged to 5×10^{-5} eV with a force tolerance of 1×10^{-2} eV/Å. When the minimum energy path was evaluated with NEB, the image structure energies were converged to 5×10^{-5} eV with a force tolerance of 5×10^{-2} eV/Å.

To provide a second evaluation of the activation energy of Ca^{2+} in the dilute concentration regime, Ab Initio Molecular Dynamics (AIMD) simulations for YVO_4 were performed in $2 \times 2 \times 2$ supercells with 1 Ca^{2+} per structure (97 atoms in total) at temperatures ranging from 600 to 1000 K. These calculations were performed with a total energy convergence criteria of 1×10^{-4} eV, a time step of 2 fs, and Gaussian smearing. The k-space was sampled with a $1 \times 1 \times 1$ γ mesh and a plane-wave cutoff of 520 eV. Lattice parameters at each temperature were determined from 3 ps-long, spin-polarized calculations with the *NPT* ensemble (constant number of atoms, pressure, and temperature) and the Langevin thermostat. The structures were then equilibrated at each temperature for 5 ps in the *NVT* ensemble (constant number of atoms, volume, and temperature) without spin polarization. *NVT* production runs were carried out for 100−200 ps with a Nosé−Hoover thermostat. In the short time span of the simulations, melting of the structures was not observed.

Synthesis of $EuCrO_4$, $YCrO_4$, $BiVO_4$, and YVO_4. $EuCrO_4$, $YCrO_4$, and YVO_4 were synthesized through a sol−gel technique using stoichiometric ratios of Eu/Cr, Y/Cr, and Y/V precursors, respectively. Europium nitrate pentahydrate $[Eu(NO_3)_3{\cdot}5H_2O]$, yttrium nitrate hexahydrate $[Y(NO_3)_3{\cdot}6H_2O]$, vanadium pentoxide (V_2O_5), and chromium(VI) oxide (CrO_3) powders were purchased from Sigma-Aldrich and used without further purification. For gelation, the powders of the transition metal source, Cr or V, were slowly dissolved in hydrogen peroxide (H_2O_2, Sigma-Aldrich). For the synthesis of YVO_4, 0.3 g of V_2O_5 were placed in a glass beaker, and 25 mL of H_2O_2 was added dropwise. The addition of H_2O_2 was done very slowly to prevent excessive bubbling and eventual loss of the material. After 10 min, a red solution was formed at which time nitrate-based $Y(NO_3)_3{\cdot}6H_2O$ was added. The amount of nitrate precursor was calculated according to the targeted 1:1 ratio of Y/V. For this purpose, 1.263 g of $Y(NO_3)_3{\cdot}6H_2O$ and 5 g of citric acid were added to the red solution. The resultant mixture was placed on a hot plate and continuously stirred at 60 °C until it formed a viscous blue-colored gel. In the final step, the gel was collected and placed in an alumina crucible and calcined at 500 °C for 30 min. The same process was applied to synthesize $YCrO_4$ and $EuCrO_4$ by changing the precursors accordingly. $BiVO_4$ was synthesized by a precipitation technique using $Bi(NO_3)_3$ and NH_4VO_3 as the precursors. The precursors were dissolved in distilled water with a stoichiometric Bi/V (1:1) ratio. The mixture was heated to 60 °C with constant stirring for 4 h. Then, 15 min of sonication was applied to the mixture. The product was used after filtration and drying at 100 °C overnight.

Electrochemical Testing. The active material, carbon black (Timcal, SUPER C65), and polytetrafluoroethylene (PTFE, DuPont, Teflon 8A) were mixed inside a glovebox at a weight ratio of 7:2:1 to prepare the cathode films. The anodes were prepared by mixing activated carbon (AC) (Sigma), carbon black, and PTFE at a weight ratio of 8:1:1 in the glovebox. The mixtures were rolled to form thin film cathodes and anodes. The coin cells were prepared using these cathode and anode thin films with a loading density of 3 mg/cm^2 cathode to 20 mg/cm^2 anode. The electrolyte was prepared by drying calcium(II) bis(trifluoromethanesulfonyl)imide [$Ca(TFSI)_2$, 99.5% Solvionic] salt at 170 °C overnight in an Ar-filled glovebox. The dried salt was then used to form 0.5 M $Ca(TFSI)_2$ in diglyme (99.5%, Sigma-Aldrich). The electrolyte and its components were kept inside the glovebox throughout the process. Coin cells were assembled using the electrolyte, cathode, and anode thin films, in addition to the separators (Whatman glass microfiber filter). Galvanostatic cycling tests were performed at 50 °C by using an Arbin battery tester. The tests were conducted at a current density of 2 mA/g, and ex situ samples were collected after washing the cathode thin films with diglyme in an Ar-filled glovebox.

X-ray Diffraction, Energy-Dispersive Spectroscopy, and Scanning Electron Microscopy Characterization. The phase identification of the synthesized samples and the structural changes in the cathodes were observed by ex situ X-ray diffraction (XRD) using a Rigaku MiniFlex 600 diffractometer with Cu Kα radiation (λ = 1.54178 Å) in the 2θ range of 10−60°. Rietveld refinement was performed using the PANalytical X'pert HighScore Plus software. Energy-dispersive spectroscopy (EDS) and scanning electron microscopy (SEM) analysis were performed on the cathode samples using a Zeiss Gemini Ultra-55 analytical field-emission scanning electron microscope at the Molecular Foundry in Lawrence Berkeley National Laboratory (LBNL).

RESULTS AND DISCUSSION

Electrode Properties Based on DFT. The calculated electrode properties of Ca zircon cathodes are shown in Table 1 and include voltages relative to Ca^{2+} metal, gravimetric capacities based on the atomic weight of the active material in the discharged state, migration barrier energies from NEB calculations in the dilute lattice limit, and volume changes upon Ca^{2+} intercalation. For comparison, calculated Mg zircon data for the same host materials are provided.[23] The notable differences include lower gravimetric capacities, higher migration barriers, and significantly larger volume changes among the Ca zircon cathodes compared to their Mg counterparts. The lower gravimetric capacity and volume change of $YCrO_4$ compared to those of $EuCrO_4$ and YVO_4 can be attributed to the lower Ca concentration.

Although there are less polarizing effects with Ca^{2+} due to its lower charge-to-volume ratio, the higher migration barriers with Ca^{2+} may be due to its preference for higher coordination numbers (e.g., 8-fold coordination) rather than an octahedral environment and the smaller cavity accommodating a larger ion such as Ca^{2+} along the transport route.[40] The barriers are consistently low in these zircons regardless of the working ion and chemical system, as well as compared to those calculated in other experimentally verified Ca cathode materials (e.g., 606

https://doi.org/10.1021/acs.chemmater.4c00062
Chem. Mater. XXXX, XXX, XXX−XXX

meV in NVPF,[8] 654 meV in CaV_2O_4,[12,14] and 1900 meV in $CaMn_2O_4$[10]) and those evaluated solely with DFT (e.g., 590 meV in $FePO_4$[15] and 500 meV in α_1-$VOPO_4$[41]). They are well below the 650 meV threshold suggested as reasonable intrinsic ionic mobility for cycling nanosized particles at a C/2 rate.[15] However, the one-dimensional tunnels may severely limit Ca diffusion since there are no alternative pathways for Ca^{2+} to travel if a channel is obstructed (e.g., by defects and impurities). The lowest NEB-confirmed Ca^{2+} migration barrier is 113 meV in YVO_4, well below the lowest reported barrier of 243 meV for intraunit diffusion in NVPF.[8] Although these $Ca_{0.5}ABO_4$ and $CaABO_4$ zircon materials boast larger gravimetric capacities than other promising cathodes studied in the literature [119−220 mA h/g in Ca zircons compared to 70−75 mA h/g in NVPF and $NaV_2(PO_4)_3$[6−8]], the large volume changes upon intercalation challenge their viability as practical Ca cathodes. In addition to this, concerns over the poor stability of magnesiated zircon compounds[23] has led us to study the Ca zircons with limited intercalation in the work below.

The energy above the hull values for 18 ABO_4 (A = [Bi, Dy, Er, Eu, Ho, La, Nd, Pr, Sm, Tb, Y], B = [Cr, V]) zircon chemical systems at two different Ca concentrations are plotted below (Figure 2). The stability of these compounds is

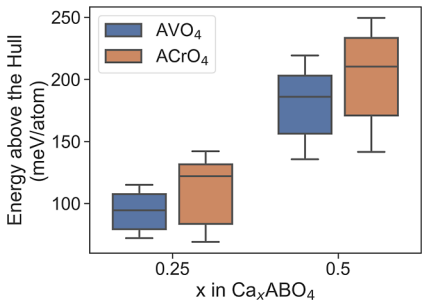

Figure 2. Phase stability of Ca_xABO_4 (x = [0.25, 0.5], A = [Bi, Dy, Er, Eu, Ho, La, Nd, Pr, Sm, Tb, Y], B = [Cr, V]) according to DFT.

measured by their energy above the hull, which is defined as the energy per atom above the convex hull, based on the MP2020 Compatibility Scheme[42] and phase diagrams that were available in the Materials Project database[28] at the beginning of this investigation. Since the convex hull represents the most stable phases in a given chemical space,[43,44] 0 meV/atom is the minimum energy above the hull and signifies that the compound of interest is the most thermodynamically stable phase at 0 K according to DFT.

On average, the discharged state energy above the hull values of $Ca_{0.25}AVO_4$ and $Ca_{0.25}ACrO_4$ are 82 and 86 meV/atom lower than those of $Ca_{0.5}AVO_4$ and $Ca_{0.5}AVO_4$, respectively. The poor stability values calculated for $Ca_{0.5}ABO_4$ are consistent with the work previously done for Mg zircon cathodes.[23] Some of the $Ca_{0.5}ABO_4$ zircons have energy above the hull values exceeding 200 meV/atom, which suggests that there is a strong driving force for these compounds to decompose into more stable phases. This has shifted the focus toward lower Ca concentrations in this cathode investigation. $Ca_{0.25}ABO_4$ stability data and decomposition products (when applicable) are tabulated in the Supporting Information (Table S1). $Ca_{0.25}LaVO_4$ and $Ca_{0.25}SmCrO_4$ are the most stable zircon vanadate and chromate at 72 and 69 meV/atom, respectively. $Ca_{0.25}$[Bi,La,Nd,Pr,Sm]VO_4 and $Ca_{0.25}$[Nd,Pr,Sm]CrO_4 have energy above the hull values below 100 meV/atom and are more likely to be synthesizable, metastable, crystalline materials than the other zircon compositions we evaluated.[31] Also, the range in stability and energy above the hull values among the calciated zircon chromates are generally higher than that of the vanadates (e.g., $Ca_{0.25}$[Nd,Dy,Y,Ho,Er]BO_4).

The electrode properties of 18 $Ca_{0.25}ABO_4$ zircons are tabulated below, with the exception of $Ca_{0.5}EuCrO_4$ due to difficulties in obtaining a stable electronic state for Eu^{3+} at lower Ca concentrations (Table 2). The following information is displayed: zircon host structure formulas, Materials Project[45] identifiers (MP-ID), intercalation and conversion reactions, voltages for these reactions, as well as the gravimetric capacities and volume changes upon intercalation. Intercalation voltages were calculated from first-principles using the total energies of the charged and discharged zircon structures.[46] Conversion voltages were also theoretically evaluated in a similar manner using pymatgen[29] and available Materials Project phase diagrams.[28]

The volume changes upon calciation are typically below 10%, which are much less significant than the values calculated in Table 1 and are comparable to volume increases in Mg zircon structures.[23] Although limited Ca^{2+} intercalation results in lower volume changes, it leads to lower gravimetric capacities ranging from 40 to 63 mA h/g, with the highest capacities found among the Y-containing chemistries due to the significantly lighter atomic weight of Y compared to that of other A site species. These values are less competitive than gravimetric capacities exceeding 70 mA h/g in high-performance Ca cathodes.[6−8] The intercalation voltages are consistently lower among the vanadates than the chromates (0.7−1.5 vs 1.8−2.1 V), and $Ca_{0.25}BiVO_4$ has a higher voltage of 1.5 V compared to the other vanadates (0.7−0.9 V). It is thermodynamically favorable for conversion reactions to take place over intercalation reactions with Ca^{2+}, as is the case for Mg^{2+}.[23] For Ca^{2+} specifically, the conversion voltages are 0.9−1.4 and 0.9−1.8 V greater than the intercalation voltages for the vanadates and chromates, respectively. Some cathodes with a larger thermodynamic driving force for conversion may be kinetically stabilized and participate in reversible intercalation reactions (e.g., Mg^{2+} in spinel Ti_2S_4[47]). However, a maximum voltage difference of $V_{conversion} - V_{intercalation}$ = 0.4 V has been experimentally verified in α-MnO_2,[48] a compound that is known to convert. Therefore, the voltage differences are too large to suggest that intercalation reactions will take place over conversion in zircon materials.

DFT-Predicted Ca-Ion Mobility. DFT-NEB calculations were carried out for YVO_4, $YCrO_4$, $BiVO_4$, and $NdCrO_4$ in the dilute lattice limit to determine the solid-state diffusion of Ca^{2+} in the zircons. The calculations confirm that the energy barriers for defect-free crystals are consistently below 250 meV across the fpur compositions studied and as low as 113 meV in YVO_4 (Figure 3). Interestingly, the compound with the best Mg-ion mobility was also identified as YVO_4 with a barrier of 71 meV.[23] These results validate the smooth energy profiles with a single saddle point at the center of the 1.6 Å migration hop, which are characteristic of nearly all of the NEB and ApproxNEB calculations for Ca zircons. The second saddle point identified in ApproxNEB image 3, predominantly in the zircon chromates, are likely artifacts due to the limitations of relaxing images independently with the approximate minimum energy path method (Figure S1). This is especially evident in

https://doi.org/10.1021/acs.chemmater.4c00062
Chem. Mater. XXXX, XXX, XXX−XXX

Table 2. Summary of the Intercalation and Conversion Electrode Properties of $Ca_{0.25}ABO_4$ (A = [Bi, Dy, Er, Ho, La, Nd, Pr, Sm, Tb, Y], B = [Cr, V]) and $Ca_{0.5}EuCrO_4$ Zircon Compounds

composition MP-ID	intercalation reaction conversion reaction	intercalation voltage conversion voltage (V vs Ca/Ca^{2+})	gravimetric capacity (mA h/g)	volume change (%)
$HoVO_4$	$0.25Ca + HoVO_4 \rightarrow Ca_{0.25}HoVO_4$	0.7	46	8
mp-18734	$14HoVO_4 + 8Ca \rightarrow V_2O_3 + 7Ho_2O_3 + 4Ca_2V_3O_8$	2.1		
$DyVO_4$	$0.25Ca + DyVO_4 \rightarrow Ca_{0.25}DyVO_4$	0.7	46	9
mp-18784	$4DyVO_4 + 2.50Ca \rightarrow 0.50CaV_2O_4 + Ca_2V_3O_8 + 2Dy_2O_3$	2.0		
$ErVO_4$	$0.25Ca + ErVO_4 \rightarrow Ca_{0.25}ErVO_4$	0.7	46	9
mp-18960	$8Ca + 14ErVO_4 \rightarrow V_2O_3 + 4Ca_2V_3O_8 + 7Er_2O_3$	2.1		
$TbVO_4$	$0.25Ca + TbVO_4 \rightarrow Ca_{0.25}TbVO_4$	0.7	47	9
mp-19121	$6Ca + 8TbVO_4 \rightarrow 3CaV_2O_4 + Ca_3V_2O_8 + 4Tb_2O_3$	2.0		
$SmVO_4$	$0.25Ca + SmVO_4 \rightarrow Ca_{0.25}SmVO_4$	0.7	49	8
mp-19323	$8SmVO_4 + 6Ca \rightarrow 4Sm_2O_3 + 3CaV_2O_4 + Ca_3V_2O_8$	1.8		
YVO_4	$0.25Ca + YVO_4 \rightarrow Ca_{0.25}YVO_4$	0.7	63	9
mp-19133	$5YVO_4 + 3Ca \rightarrow 3YVO_3 + Y_2O_3 + Ca_3V_2O_8$	2.1		
$NdVO_4$	$0.25Ca + NdVO_4 \rightarrow Ca_{0.25}NdVO_4$	0.8	50	5
mp-18812	$6Ca + 8NdVO_4 \rightarrow 3CaV_2O_4 + Ca_3V_2O_8 + 4Nd_2O_3$	1.8		
$PrVO_4$	$0.25Ca + PrVO_4 \rightarrow Ca_{0.25}PrVO_4$	0.9	50	5
mp-19169	$Ca + PrVO_4 \rightarrow CaO + PrVO_3$	1.8		
$LaVO_4$	$0.25Ca + LaVO_4 \rightarrow Ca_{0.25}LaVO_4$	0.9	51	5
mp-19162	$LaVO_4 + Ca \rightarrow CaO + LaVO_3$	1.8		
$BiVO_4$	$0.25Ca + BiVO_4 \rightarrow Ca_{0.25}BiVO_4$	1.5	40	12
mp-545850	$3Ca + 9BiVO_4 \rightarrow 3CaVBiO_5 + V_3O_5 + V_3(Bi_3O_8)_2$	2.6		
$ErCrO_4$	$0.25Ca + ErCrO_4 \rightarrow Ca_{0.25}ErCrO_4$	1.8	46	9
mp-19240	$2Ca + 5ErCrO_4 \rightarrow Er_2O_3 + 3ErCrO_3 + 2CaCrO_4$	3.6		
$DyCrO_4$	$0.25Ca + DyCrO_4 \rightarrow Ca_{0.25}DyCrO_4$	1.9	46	9
mp-18754	$1.33Ca + 3.33DyCrO_4 \rightarrow Cr_2O_3 + 1.66Dy_2O_3 + 1.33CaCrO_4$	3.4		
$HoCrO_4$	$0.25Ca + HoCrO_4 \rightarrow Ca_{0.25}HoCrO_4$	1.9	46	9
mp-19076	$1.33Ca + 3.33HoCrO_4 \rightarrow 1.66Ho_2O_3 + Cr_2O_3 + 1.33CaCrO_4$	3.5		
$YCrO_4$	$0.25Ca + YCrO_4 \rightarrow Ca_{0.25}YCrO_4$	1.9	62	9
mp-18825	$2Ca + 5YCrO_4 \rightarrow Y_2O_3 + 3YCrO_3 + 2CaCrO_4$	3.5		
$SmCrO_4$	$0.25Ca + SmCrO_4 \rightarrow Ca_{0.25}SmCrO_4$	2.0	48	6
mp-18956	$1.33Ca + 3.33SmCrO_4 \rightarrow 1.66Sm_2O_3 + Cr_2O_3 + 1.33CaCrO_4$	3.1		
$EuCrO_4$	$0.50Ca + EuCrO_4 \rightarrow Ca_{0.5}EuCrO_4$	2.0	93	18
mp-22586	$5EuCrO_4 + 2Ca \rightarrow 3EuCrO_3 + Eu_2O_3 + 2CaCrO_4$	3.0		
$PrCrO_4$	$0.25Ca + PrCrO_4 \rightarrow Ca_{0.25}PrCrO_4$	2.1	50	5
mp-18863	$4PrCrO_4 + 2.50Ca \rightarrow 1.50CaCr_2O_4 + 2Pr_2O_3 + CaCrO_4$	3.0		
$NdCrO_4$	$0.25Ca + NdCrO_4 \rightarrow Ca_{0.25}NdCrO_4$	2.1	50	5
mp-19126	$2Ca + 5NdCrO_4 \rightarrow 3NdCrO_3 + Nd_2O_3 + 2CaCrO_4$	3.3		

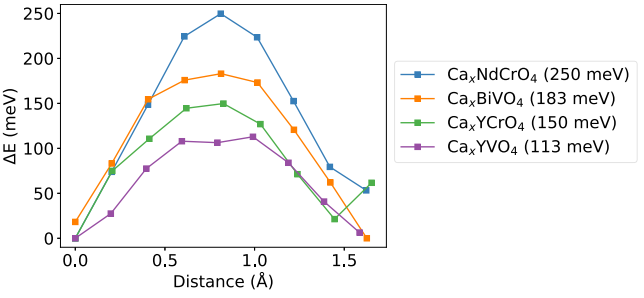

Figure 3. DFT-NEB energy profiles for Ca_xYVO_4, Ca_xYCrO_4, Ca_xBiVO_4, and Ca_xNdCrO_4 in the dilute lattice limit ($x \leq 0.06$ with 1 Ca-ion per supercell structure).

$NdCrO_4$, which has a NEB barrier of 250 meV and an ApproxNEB barrier of 367 meV due to the higher relative energy of ApproxNEB image 3. The larger site volume of Ca^{2+}, which is defined as the volume enclosed by an atom's corresponding Voronoi polyhedron,[49,50] in $NdCrO_4$ Approx-NEB image structures 2 through 6 compared to those of their respective NEB images indicate that the image structures relaxed differently and may contribute to the discrepancies in energy.

While it is expected for ApproxNEB barriers to exceed those of NEB due to the lower number of degrees of freedom explored during the decoupled relaxations of the approximate method,[32] the migration barriers calculated with ApproxNEB are greater than or nearly equal to the NEB barriers for all candidates except YVO_4. To further investigate this disagreement, the coordination environment of Ca^{2+} was evaluated using the CrystalNN algorithm[50] as implemented in pymatgen.[29] Greater differences in the energetic landscape between the two methods are observed when the local environment around Ca^{2+} changes significantly (e.g., coordi-

https://doi.org/10.1021/acs.chemmater.4c00062
Chem. Mater. XXXX, XXX, XXX−XXX

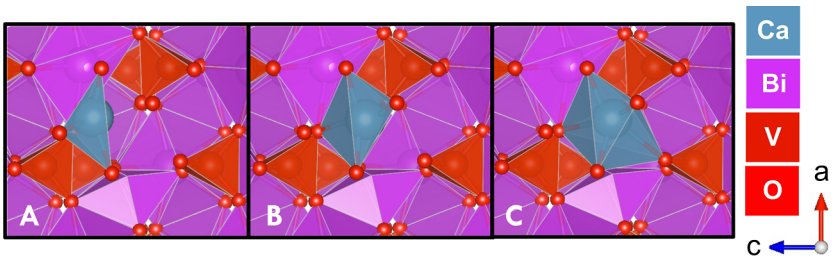

Figure 4. Low coordination change of Ca^{2+} in DFT-relaxed NEB image structures of Ca_xBiVO_4. Ca^{2+} has coordination values of 4, 5, and 6 with oxygen in images A, B, and C, respectively. Ca^{2+} diffuses along the *c*-axis in the one-dimensional channel.

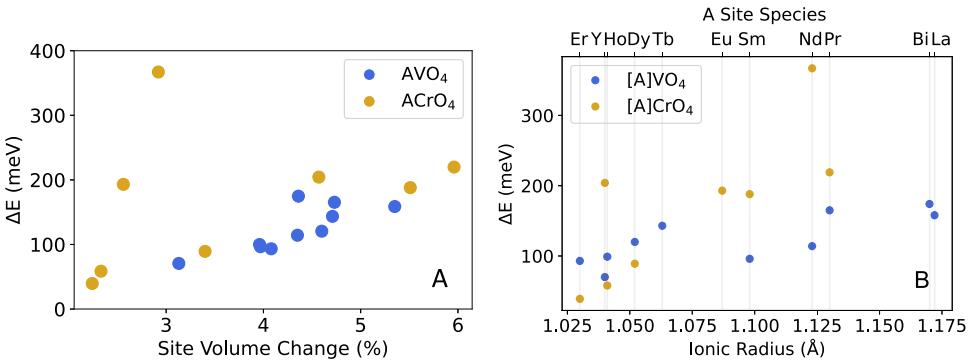

Figure 5. (A) Site volume change of Ca^{2+} at the metastable intercalation site vs the transition state site as a function of DFT-ApproxNEB energy barrier in the dilute lattice limit. Results are plotted for Ca_xACrO_4 in yellow and Ca_xAVO_4 in blue ($x \leq 0.06$ with 1 Ca-ion per supercell structure, A = [Bi, Dy, Er, Eu, Ho, La, Nd, Pr, Sm, Tb, Y]). (B) ApproxNEB barriers of the chromate (in yellow) and vanadate (in blue) zircons as a function of the ionic radii of the A site species in ABO_4, which are labeled by element at the top of the plot.

nation increase of 6 to 7 between adjacent NEB images vs a decrease of 6 to 4 between adjacent ApproxNEB images). As a result, the low barrier difference of 8 meV between the ApproxNEB and NEB results for $BiVO_4$ is explained by the nearly identical coordination values of Ca^{2+} across the NEB and ApproxNEB image structures. Although site volume and coordination analysis do not provide a clear explanation for the underestimated ApproxNEB barrier for Ca^{2+} migration in YVO_4, the lowest Ca^{2+} migration barrier of 113 meV is confirmed in YVO_4 with NEB.

The coordination change of Ca^{2+} was analyzed in DFT-relaxed NEB image structures to compare to the "6-5-4" coordination pattern found in Mg zircon cathodes.[23] The same structural motif was identified in Ca zircon materials (Figure 4) and explains the low migration barriers with multiple working ions in this family of materials.[20] Since there is a recurring overlap of interstitial distorted tetrahedral and octahedral sites in the one-dimensional diffusion channel, the resulting smooth coordination change reduces the interstitial site preference and allows for good solid-state mobility in zircons. The "6-5-4" motif is a more gradual change in coordination compared to the "6-3-4" theme identified in migration paths for close-packed oxides, where the mobile species travels from either a tetrahedral to octahedral or octahedral to tetrahedral interstitial site and crosses through a face coordinated with three oxygen.[15] It is more favorable to travel through a coordination of 5 rather than 3 because ion migration through a plane of anions has been correlated with higher energy barriers.[27] This is also consistent with reports in the literature on Mg electrodes with reversible intercalation that have prototype structures with low coordination change for Mg^{2+} (e.g., chevrel Mo_6S_8,[51] layered MoO_3, and orthorhombic V_2O_5[52]), as well as analysis of coordination change increasing site energy differences along the diffusion path and the resulting migration barrier in multivalent cathode materials.[15]

In addition to DFT-NEB, DFT-ApproxNEB calculations were performed for 18 zircon candidates to evaluate the Ca-ion mobility in the ABO_4 family in the dilute lattice limit. All 18 ApproxNEB energy barriers are below 370 meV and confirm the potential for fast Ca-ion transport across compositions. To investigate the relationship between local environment changes and Ca-ion mobility, the change between the Ca^{2+} site volume at the metastable intercalation site (V_i) and at the transition state site (V_{TS}) was calculated as follows: $(V_{TS} - V_i)/V_i$. These site volume changes are plotted as a function of the ApproxNEB energy barrier for the studied zircon chromates and vanadates (Figure 5A). There is a positive correlation between the change in site volume and migration barrier, which agrees with similar analysis on the diffusion of Na^+, Ca^{2+}, Mg^{2+}, and Zn^{2+} in zircon conductors.[20] However, increases in the Ca site volume as the mobile ion travels from the metastable to the transition state site are observed, and surprisingly, the lowest site volume does not correspond to the bottleneck in migration along the pathway. It is believed that the larger variations in site volume result in higher energy barriers due to more significant changes in the local environment around Ca^{2+} and stronger preferences for site occupation.[15] $EuCrO_4$ and $NdCrO_4$ present themselves as outliers (site volume changes of 2.6, 2.9%, and barriers of 193 and 367 meV, respectively) due to the misleading identification of additional saddle points with ApproxNEB in zircon chromates as discussed above.

Although the site volume of Ca^{2+} is larger at the transition state site, we confirm the well-known inverse relationship between ΔE and the nearest cation distance to Ca^{2+} in all 18

https://doi.org/10.1021/acs.chemmater.4c00062
Chem. Mater. XXXX, XXX, XXX−XXX

zircon candidates (Figure S2). The nearest framework atom species is either Cr or V, depending on the zircon composition, along the migration pathway, when the ΔE is at its maximum. Nearby cations destabilize the structure and the greater Coulombic forces interacting with Ca^{2+} contribute to higher energy barriers. Since the main difference among the materials studied is their composition, the influence of the A site species in ABO_4 was investigated in the context of Ca-ion mobility. ApproxNEB barriers are plotted as a function of these ionic radii (Figure 5B) and show a weak trend for zircon materials with larger A elements to exhibit higher migration energies. A slightly more positive correlation between the energy barriers and ionic radii is present in the chromates than in the vanadates. Since Ca^{2+} consistently has a larger site volume in zircon materials with A site species of greater ionic radii as well as longer lattice parameters (Figure S3), it is hypothesized that the longer lattice parameters increase with the Ca^{2+} migration barriers. This counterintuitive phenomenon has been seen in several studies on lattice expansion impairing ion mobility due to local bonding effects on ion transport[53−55] and supports our observations in Ca zircon materials. As a result, there is a weak but positive correlation between the ionic mobility of Ca^{2+} and the intercalation voltages. This can be attributed to the influence of the A site species and size on both the migration barrier and the thermodynamic stability of the intercalated material, which affects the theoretical voltage.

AIMD simulations were also carried out for Ca_xYVO_4 in the dilute lattice limit to confirm the DFT-NEB and DFT-ApproxNEB migration barriers in addition to the one-dimensional transport tunnel identified with the insertion algorithm and migration graph analysis. Diffusion properties and their corresponding error values were calculated with an empirical relation between the diffusion coefficient's relative standard deviation and the total mean squared displacement.[56] The activation energy is 108 ± 18 meV based on the Arrhenius relationship between the diffusivity and temperature, which is consistent with the energy barrier derived from NEB for YVO_4. Furthermore, the diffusivity projected from the Arrhenius relation and higher temperature data agrees with the diffusivity of 6.9×10^{-6} cm^2/s based on AIMD simulations at 300 K (Figure 6), indicating no significant difference between the

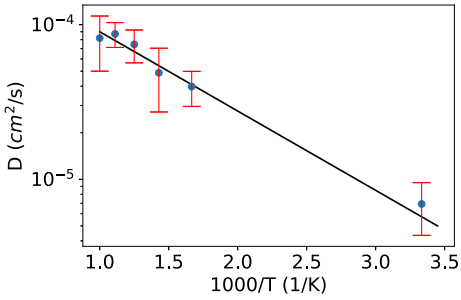

Figure 6. Arrhenius plot of Ca diffusivity in YVO_4 in the dilute lattice limit (0.03 Ca^{2+} per ABO_4 formula unit) from AIMD simulations.

low- and high-temperature transport mechanisms. Probability density analysis of the AIMD data was performed with the python package pymatgen-diffusion[57] and supports Ca-ion diffusion in the one-dimensional transport channel along the *c*-axis. There was no evidence of Ca^{2+} migration between channels throughout 200 ps of AIMD simulations (Figure S4). However, we note that 200 ps is insufficient to rule out the presence of defects especially in larger particles. The low dimensionality of the migration pathway is likely to result in capacity loss due to channel blocking (e.g., by native antisite defects, impurities).[58]

Although the concentration of the mobile species has affected the energy barrier in systems such as Mg_xFePO_4 (580 meV in the dilute limit vs 1025 meV in $Mg_{0.5}FePO_4$[59]), we believe the bottleneck for Ca^{2+} intercalation is the poor phase stability at higher concentrations. First of all, the Ca−Ca distance within the confirmed one-dimensional diffusion channel in $Ca_{0.25}ABO_4$ is much greater than the Mg−Mg distance in $Mg_{0.5}FePO_4$ (12.4−12.6 vs 5.0 Å). The low density of Ca^{2+} in the zircon channels suggests that the coordination of one Ca^{2+} atom is not affected by nearby Ca^{2+} atoms, preserving the structural motif for good ion mobility. Furthermore, the energy above the hull values for $Ca_{0.25}ABO_4$ range from 69 to 142 meV/atom, and they are well above 125 meV/atom at higher concentrations such as $Ca_{0.5}ABO_4$. While the minimum energy pathways were evaluated in the dilute lattice limit, we believe that the energy barriers will remain largely unchanged in $Ca_{0-0.25}ABO_4$, which is the concentration range of interest.

Defect Analysis with DFT. The poor phase stability of the discharged Ca zircons may be attributed to the unfavorable coordination environment of the B site transition metal in ABO_4 zircon materials. The tetrahedrally coordinated redox-active transition metal (Cr, V) favors octahedral coordination when reduced (e.g., V^{5+} to $V^{3+,4+}$, $Cr^{5+,6+}$ to $Cr^{3+,4+}$).[60] To explore the possibility of increased channel blocking by the transition metal upon reduction, Ca−V antisite defect formation energies were calculated in YVO_4 at several Ca concentrations. Since there are multiple atomic configurations for Ca^{2+} intercalation sites in $Ca_{0.5}YVO_4$ and $CaYVO_4$, 50 symmetrically unique supercell structures with low Ewald energy were generated using pymatgen.[29] The structure with the lowest total energy from DFT relaxations was selected for the subsequent step, where atomic positions were exchanged in one pair of Ca^{2+} and its closest neighboring V^{3-5+} (Figure 7).

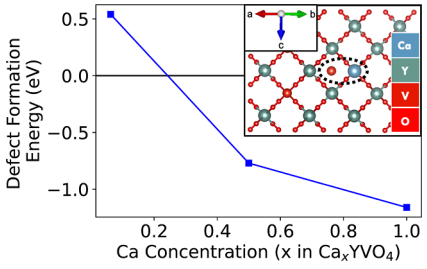

Figure 7. Ca−V defect formation energies in Ca_xYVO_4 (x = [0.0625, 0.5, 1]) derived from DFT-relaxed supercell structures. The Ca−V defect pair is circled in Ca_xYVO_4 in the dilute lattice limit, with V^{5+} situated in the one-dimensional transport channel that is in/out of the page.

Total energies were evaluated with DFT relaxations for the pristine and defect-containing structure at each Ca concentration, and the defect formation energies ($E_{f,defect}$) were calculated as follows: $E_{f,defect} = E_{t,defect} - E_{t,pristine}$. We find that it is not energetically favorable for V^{5+}/Ca^{2+} to form an antisite defect with V^{5+} residing in the one-dimensional diffusion channel (Figure 7). However, when V^{5+} is reduced to V^{4+} and V^{3+} in $Ca_{0.5}YVO_4$ and $CaYVO_4$, respectively, the structure with the Ca−V defect is more stable than the pristine material and

https://doi.org/10.1021/acs.chemmater.4c00062
Chem. Mater. XXXX, XXX, XXX−XXX

validates the concern of intercalating Ca^{2+} and Mg^{2+} at higher concentrations.

Experimental Synthesis of Ca Zircon Materials. Previous sol−gel synthesis work on YVO_4 nano powders[61] was adapted to synthesize three ABO_4 compounds (YVO_4, $EuCrO_4$, and $YCrO_4$) with oxide precursors (CrO_3 and V_2O_5) as the source of B site transition metals, and nitrate-based precursors as the source of A site cations (Eu^{3+} and Y^{3+}). The sol−gel method was unsuccessful for $BiVO_4$ because the scheelite polymorph was obtained during synthesis instead of the tetragonal zircon-type structure. However, $BiVO_4$ synthesis was pursued despite this complication because it was predicted to have a higher theoretical voltage of 1.5 V versus Ca/Ca^{2+} compared to the other zircon vanadates (0.7−0.9 V). Thus, a simple precipitation technique was applied to synthesize $BiVO_4$ nanopowders.[62] Details for this synthesis technique can be found in the "Methods" section. The phase purity of the samples was verified through ex situ XRD studies and subsequent Rietveld refinement analysis (Figure 8). The

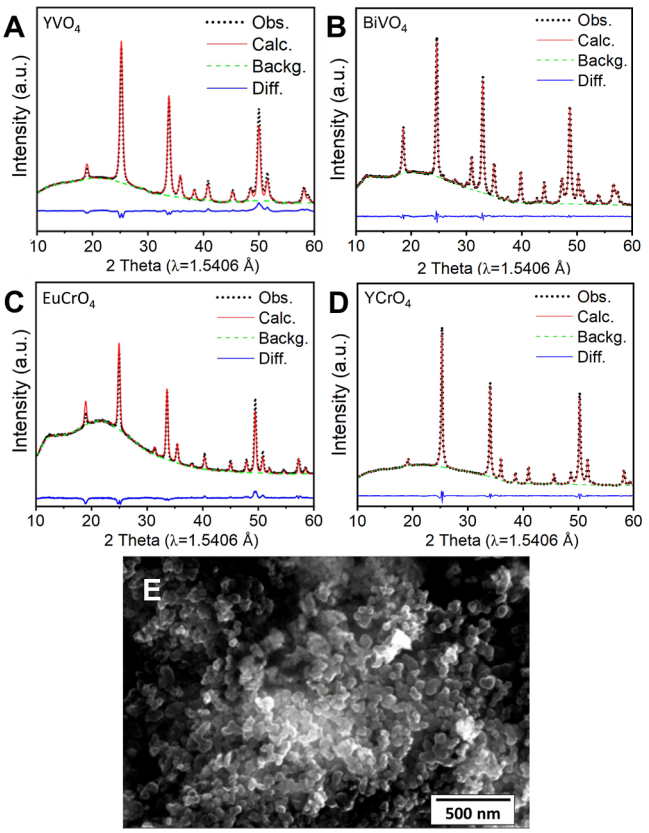

Figure 8. XRD results of the as-synthesized (A) YVO_4, (B) $BiVO_4$, (C) $EuCrO_4$, and (D) $YCrO_4$ compounds. (E) SEM image of the YVO_4 powder after calcination at 500 °C for 30 min.

corresponding XRD patterns of YVO_4, $BiVO_4$, $EuCrO_4$, and $YCrO_4$ indicate high phase purity in all of the samples. The high and broad baseline at lower 2θ values is attributed to the Kapton tape that covered the samples to minimize air exposure. During synthesis, the calcination time was fixed at 30 min and at a temperature of 500 °C. This method is more advantageous to obtain small and homogeneously distributed particles compared to classical solid-state synthesis techniques, which may require longer sintering times (20−30 h) at higher temperatures (e.g., 800 °C). The SEM images of the samples revealed that the samples have a homogeneous particle size distribution with an average particle size range of 50−60 nm, and therefore compounds other than Ca_xABO_4 do not appear to have formed.

Electrochemical Cycling of Ca Zircon Cathodes. The charge and discharge profiles of the cells were measured in a coin cell structure against an AC anode and customized electrolyte [0.5 M $Ca(TFSI)_2$ in diglyme] at 50 °C with a current density of 2 mA/g. This setup and its cell components allowed measurements in the voltage range of −2 to 1.2 V versus AC. The electrolyte was stable in this voltage window. Although the electrochemical data demonstrate that the compounds showed slightly different behavior upon cycling, the cycles' overall reversibility suggests that Ca^{2+} intercalation predominantly contributes to the measured capacities over other reactions such as conversion (Figure 9). Under the same testing conditions, the first discharge capacities were measured as 81, 65, 60, and 72 mA h/g for YVO_4, $BiVO_4$, $EuCrO_4$, and $YCrO_4$, respectively. In the subsequent charging cycle, the specific capacities were measured as 68, 62, 60, and 60 mA h/g for YVO_4, $BiVO_4$, $EuCrO_4$, and $YCrO_4$, respectively. Significant portions of the first discharge capacities could not be recovered in the cases of $YCrO_4$ and YVO_4, while $EuCrO_4$ and $BiVO_4$ showed almost full recovery. In the following cycles, excess discharge capacities were observed, which indicates possible side reactions in the low voltage regime. YVO_4 achieved the highest specific capacity, while the best reversibility was realized with $BiVO_4$. The lower DFT-calculated energy above the hull value for $BiVO_4$ in the discharged state may be responsible for its superior cyclability compared to the other candidates that were studied experimentally.

Although YVO_4 exhibited better performance compared to $EuCrO_4$ upon electrochemical cycling with Mg^{2+},[23] $EuCrO_4$ demonstrated more reversible cycling with Ca^{2+} than YVO_4 after five charge and discharge cycles. The poorer cycle reversibility in YVO_4 is not attributed to bulk phase transitions upon Ca^{2+} intercalation because ex situ XRD confirmed its structure remained in the tetragonal zircon crystalline phase after charge and discharge. However, it is important to note the possibility of amorphous products (especially at the particle surface) and partial dissolution of the material in the electrolyte that may not have been captured with XRD. Overall, the Ca zircon samples achieved similar intercalation voltages and slightly higher capacities compared to Mg zircon cathodes, which may be due in part to the limitations of the electrolyte (narrower voltage window of −1.5 to −1.1 V vs AC for Mg^{2+} compared to −2 to −1.2 V vs AC for Ca^{2+}). These experimental results broadly support the theoretically predicted capacities and voltages for Ca zircon materials, with the exception of higher average closed-circuit voltages (CCVs) for the zircon vanadates compared to their voltages calculated from first-principles (1.9 vs 0.7 V for YVO_4 and 2.0 vs 1.5 V for $BiVO_4$). A comparison between the voltages computed with DFT and the average open-circuit voltages (OCVs) measured at the beginning of each discharge and charge cycle yielded similar results (Table S2). The discrepancy between the experimental and theoretical voltages is also reported in Mg zircons.[23] It may be a result of higher overpotentials during Ca^{2+} removal or of measuring the voltages relative to an AC anode in experiments, which may not accurately correspond to voltage values relative to a Ca metal anode.

https://doi.org/10.1021/acs.chemmater.4c00062
Chem. Mater. XXXX, XXX, XXX−XXX

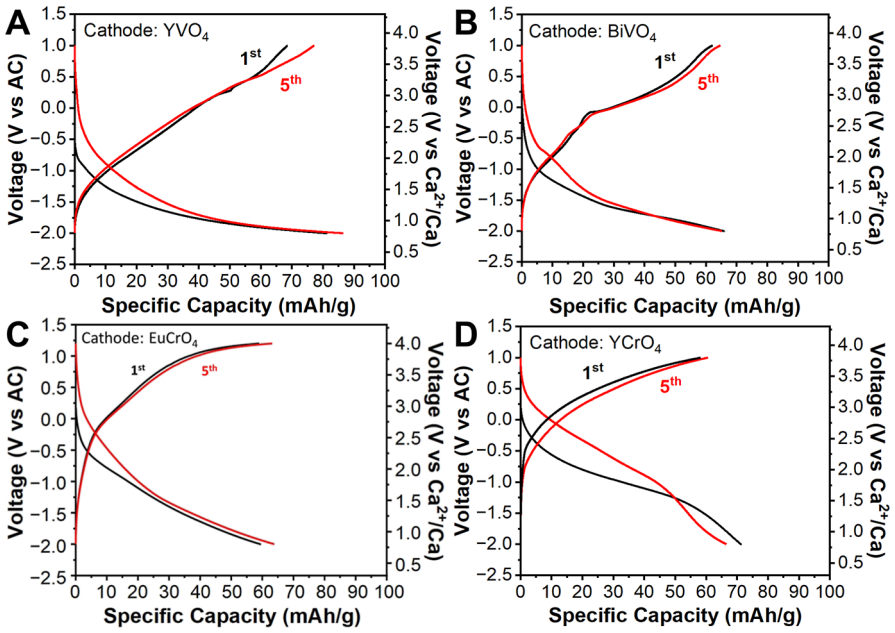

Figure 9. Charge and discharge voltage profiles of (A) YVO_4, (B) $BiVO_4$, (C) $EuCrO_4$, and (D) $YCrO_4$ cathodes relative to an AC anode at 50 °C with a current density of 2 mA/g.

Table 3. Elemental Compositions of the Ex Situ Samples Measured by SEM−EDS Analysis after the 1st Charge and 1st Discharge Cycle

	atomic percentages (%)							
	$EuCrO_4$		YVO_4		$YCrO_4$		$BiVO_4$	
	disch.	charged	disch.	charged	disch.	charged	disch.	charged
Ca	9.83	0.72	10.40	0.86	11.44	0.85	11.30	0.65
A (Eu, Y, Bi)	43.85	47.96	46.24	49.52	46.48	49.63	46.44	49.66
B (V, Cr)	46.32	51.32	44.06	49.32	44.07	59.62	42.87	59.69

SEM−EDS Characterization of Ca Zircons. The compositions of $EuCrO_4$, $YCrO_4$, YVO_4, and $BiVO_4$ were measured via ex situ SEM−EDS with fresh coin cells after the 1st charge and 1st discharge cycle to verify Ca^{2+} intercalation (Table 3). The SEM−EDS results show that Ca^{2+} is successfully intercalated after the 1st discharge to −2.0 V versus AC and removed again after the 1st charge with 1 at. % or less remaining in the four samples. Higher Ca atomic percentages are present in the discharged zircon vanadates than in the chromates, with the most significant intercalation achieved in $BiVO_4$ with 14.20 at. %, consistent with its more favorable, theoretically predicted phase stability. Upon comparing our Ca SEM−EDS results with those reported for Mg zircons,[23] there is a noticeably higher Ca^{2+} content compared to that of Mg^{2+}, with 9.83 vs 6.24 at. % in $EuCrO_4$ and 11.34 vs 8.94 at. % in YVO_4 for Ca^{2+} and Mg^{2+}, respectively. The data in Table 3 suggest that $Ca_{0.20}EuCrO_4$, $Ca_{0.20}YCrO_4$, $Ca_{0.24}YVO_4$, and $Ca_{0.31}BiVO_4$ were obtained experimentally after discharging with Ca^{2+}. The experimentally observed Ca^{2+} intercalation limits are consistent with the electrochemically measured capacities, and they generally align with the theoretical prediction that the discharged material becomes too unstable beyond $Ca_{0.25}ABO_4$.

CONCLUSIONS

ABO_4 zircons were evaluated as possible Ca cathode materials through a series of DFT-based criteria as well as experimental synthesis, characterization, and electrochemical testing. Ca solid-state mobility was approximately evaluated for 18 zircon candidates (A = [Bi, Dy, Er, Eu, Ho, La, Nd, Pr, Sm, Tb, Y], B = [Cr, V]) and more precisely calculated for YVO_4, $YCrO_4$, $BiVO_4$, and $NdCrO_4$. The lowest Ca^{2+} migration barrier among the zircons is 113 meV in YVO_4 based on NEB calculations, with an estimated activation energy of 108 meV at room temperature according to AIMD simulations. To the best of our knowledge, this is the lowest Ca^{2+} migration barrier reported in the literature. Furthermore, remarkably high Ca-ion mobility is predicted in all of the defect-free zircon materials that were studied, with migration barriers consistently below 300 meV. We attribute this to the smooth coordination change and reduced site preference for Ca^{2+}. However, AIMD simulations confirm that the migration pathway is a one-dimensional channel (Figure S4), raising concerns over channel-blocking mechanisms that may significantly impair Ca diffusion.

Four zircon candidates were experimentally tested and are found to successfully intercalate Ca^{2+}. Initial gravimetric capacities as high as 81 mA h/g were achieved with average voltages of 1.9−2.3 V versus Ca/Ca^{2+}. While these experimentally measured voltages are lower relative to state-of-the-art Ca cathodes with voltages around 3.2 V, this work demonstrates the viability of computational evaluation, specifically in identifying "empty host" materials with excellent structural ionic mobility motifs. Further investigations of structures with zircon-like motifs and chemical systems with

https://doi.org/10.1021/acs.chemmater.4c00062
Chem. Mater. XXXX, XXX, XXX−XXX

higher voltages are encouraged. The best reversibility among the selected compounds studied was demonstrated in $BiVO_4$. Despite the promising Ca-ion mobility in zircons, intercalation may be limited due to the poor phase stability of the discharged materials. Although conversion reactions and/or amorphization are not explicitly observed by characterization techniques used in this investigation, they are found to be thermodynamically favorable. Defect calculations also corroborate the hypothesis that the unfavorable coordination environment of the redox B site species destabilizes the structure, especially at higher Ca concentrations.

Interestingly, the unique pattern of overlapping octahedral sites by tetrahedral interstitial sites in zircon materials is shown to support facile Ca^{2+} transport. Given that good Mg-ion mobility in zircons has been demonstrated in the literature,[23] this structural motif is a highly versatile feature for fast ionic transport design. Further theoretical and experimental studies of zircon materials may be warranted to identify the most optimal candidate across the zircon family's wide chemical space, such as a high voltage, Ca zircon chromate material equivalent to Ca_xBiVO_4.

■ ASSOCIATED CONTENT

Supporting Information

The Supporting Information is available free of charge at https://pubs.acs.org/doi/10.1021/acs.chemmater.4c00062.

DFT-predicted energy above the hull values for $Ca_{0.25}ABO_4$ (A = [Bi, Dy, Er, Ho, La, Nd, Pr, Sm, Tb, Y], B = [Cr, V]) and $Ca_{0.5}EuCrO_4$; DFT-ApproxNEB energy profiles for Ca_xABO_4 ($x \leq 0.06$, A = [Bi, Dy, Er, Eu, Ho, La, Nd, Pr, Sm, Tb, Y], B = [Cr, V]) in the dilute lattice limit; DFT-ApproxNEB energy profile juxtaposed with the nearest cation distance to Ca^{2+} for Ca_xYVO_4; site volume of Ca^{2+} at the metastable intercalation site and at the transition state site as a function of ionic radius of the A site species in ApproxNEB supercell structures; AIMD probability density analysis for Ca^{2+} in YVO_4 at 600 K in the dilute limit; and comparison between average voltages calculated from first-principles, average CCVs, and average OCVs for YVO_4, $BiVO_4$, $EuCrO_4$, and $YCrO_4$ (PDF)

■ AUTHOR INFORMATION

Corresponding Author

Kristin A. Persson − *Department of Materials Science and Engineering, University of California, Berkeley, California 94704, United States; Materials Sciences Division, Lawrence Berkeley National Laboratory, Berkeley, California 94720, United States; Molecular Foundry, Lawrence Berkeley National Laboratory, Berkeley, California 94720, United States*; Email: kapersson@lbl.gov

Authors

Jiyoon Kim − *Department of Materials Science and Engineering, University of California, Berkeley, California 94704, United States; Materials Sciences Division, Lawrence Berkeley National Laboratory, Berkeley, California 94720, United States;* orcid.org/0000-0002-0383-1198

Dogancan Sari − *Department of Materials Science and Engineering, University of California, Berkeley, California 94704, United States; Materials Sciences Division, Lawrence Berkeley National Laboratory, Berkeley, California 94720, United States*

Qian Chen − *Materials Sciences Division, Lawrence Berkeley National Laboratory, Berkeley, California 94720, United States;* orcid.org/0009-0009-3557-0744

Ann Rutt − *Department of Materials Science and Engineering, University of California, Berkeley, California 94704, United States; Materials Sciences Division, Lawrence Berkeley National Laboratory, Berkeley, California 94720, United States;* orcid.org/0000-0001-6534-454X

Gerbrand Ceder − *Department of Materials Science and Engineering, University of California, Berkeley, California 94704, United States; Materials Sciences Division, Lawrence Berkeley National Laboratory, Berkeley, California 94720, United States;* orcid.org/0000-0001-9275-3605

Complete contact information is available at: https://pubs.acs.org/10.1021/acs.chemmater.4c00062

Notes

The authors declare no competing financial interest.

■ ACKNOWLEDGMENTS

This work was supported by the Volkswagen Group and the National Science Foundation under grant no. 2146752. Materials data and software infrastructure support were provided by the Materials Project, which is funded by the U.S. Department of Energy, Office of Science, Office of Basic Energy Sciences, Materials Sciences and Engineering Division, under contract no. DE-AC02-05-CH11231: Materials Project Program KC23MP. This research used computational resources provided by the National Energy Research Scientific Computing Center (NERSC), a U.S. Department of Energy Office of Science User Facility operated under contract no. DE-AC02-05-CH11231. The work of D.S. was supported by a Fulbright Program grant sponsored by the Bureau of Educational and Cultural Affairs of the United States Department of State and administered by the Institute of International Education.

■ REFERENCES

(1) Nykvist, B.; Nilsson, M. Rapidly falling costs of battery packs for electric vehicles. *Nat. Clim. Change* **2015**, *5*, 329−332.

(2) Sarma, D. D.; Shukla, A. K. Building Better Batteries: A Travel Back in Time. *ACS Energy Lett.* **2018**, *3*, 2841−2845.

(3) Ponrouch, A.; Palacín, M. R. Post-Li batteries: promises and challenges. *Philos. Trans. R. Soc., A* **2019**, *377*, 20180297.

(4) Gummow, R. J.; Vamvounis, G.; Kannan, M. B.; He, Y. Calcium-Ion Batteries: Current State-of-the-Art and Future Perspectives. *Adv. Mater.* **2018**, *30*, 1801702.

(5) Wang, D.; Gao, X.; Chen, Y.; Jin, L.; Kuss, C.; Bruce, P. G. Plating and stripping calcium in an organic electrolyte. *Nat. Mater.* **2018**, *17*, 16−20.

(6) Kim, S.; Yin, L.; Lee, M. H.; Parajuli, P.; Blanc, L.; Fister, T. T.; Park, H.; Kwon, B. J.; Ingram, B. J.; Zapol, P.; Klie, R. F.; Kang, K.; Nazar, L. F.; Lapidus, S. H.; Vaughey, J. T. High-Voltage Phosphate Cathodes for Rechargeable Ca-Ion Batteries. *ACS Energy Lett.* **2020**, *5*, 3203−3211.

(7) Jeon, B.; Heo, J. W.; Hyoung, J.; Kwak, H. H.; Lee, D. M.; Hong, S. T. Reversible calcium-ion insertion in NaSICON-type NaV2(PO4)3. *Chem. Mater.* **2020**, *32*, 8772−8780.

(8) Xu, Z.-L.; Park, J.; Wang, J.; Moon, H.; Yoon, G.; Lim, J.; Ko, Y.-J.; Cho, S.-P.; Lee, S.-Y.; Kang, K. A new high-voltage calcium intercalation host for ultra-stable and high-power calcium rechargeable batteries. *Nat. Commun.* **2021**, *12*, 3369.

(9) Zhang, Z.; Zhang, X.; Zhao, X.; Yao, S.; Chen, A.; Zhou, Z. Computational Screening of Layered Materials for Multivalent Ion Batteries. *ACS Omega* **2019**, *4*, 7822−7828.
(10) Dompablo, M. E. A.-d.; Krich, C.; Nava-Avendaño, J.; Biškup, N.; Palacín, M. R.; Bardé, F. A Joint Computational and Experimental Evaluation of CaMn2O4 Polymorphs as Cathode Materials for Ca Ion Batteries. *Chem. Mater.* **2016**, *28*, 6886−6893.
(11) Liu, M.; Rong, Z.; Malik, R.; Canepa, P.; Jain, A.; Ceder, G.; Persson, K. A. Spinel compounds as multivalent battery cathodes: a systematic evaluation based on ab initio calculations. *Energy Environ. Sci.* **2015**, *8*, 964−974.
(12) Lu, W.; Wang, J.; Sai Gautam, G.; Canepa, P. Searching Ternary Oxides and Chalcogenides as Positive Electrodes for Calcium Batteries. *Chem. Mater.* **2021**, *33*, 5809−5821.
(13) Bölle, F. T.; Mathiesen, N. R.; Nielsen, A. J.; Vegge, T.; Garcia-Lastra, J. M.; Castelli, I. E. Autonomous Discovery of Materials for Intercalation Electrodes. *Batteries Supercaps* **2020**, *3*, 488−498.
(14) Black, A. P.; Frontera, C.; Torres, A.; Recio-Poo, M.; Rozier, P.; Forero-Saboya, J. D.; Fauth, F.; Urones-Garrote, E.; Arroyo-de Dompablo, M. E.; Palacín, M. R. Elucidation of the redox activity of Ca2MnO3.5 and CaV2O4 in calcium batteries using operando XRD: charge compensation mechanism and reversibility. *Energy Storage Mater.* **2022**, *47*, 354−364.
(15) Rong, Z.; Malik, R.; Canepa, P.; Sai Gautam, G.; Liu, M.; Jain, A.; Persson, K.; Ceder, G. Materials Design Rules for Multivalent Ion Mobility in Intercalation Structures. *Chem. Mater.* **2015**, *27*, 6016−6021.
(16) Panchal, V.; Errandonea, D.; Segura, A.; Rodríguez-Hernandez, P.; Muñoz, A.; Lopez-Moreno, S.; Bettinelli, M. The electronic structure of zircon-type orthovanadates: Effects of high-pressure and cation substitution. *J. Appl. Phys.* **2011**, *110*, 043723.
(17) Huang, Z.; Feng, J.; Pan, W. Theoretical investigations of the physical properties of zircon-type YVO4. *J. Solid State Chem.* **2012**, *185*, 42−48.
(18) Errandonea, D.; Kumar, R.; López-Solano, J.; Rodríguez-Hernández, P.; Muñoz, A.; Rabie, M. G.; Sáez Puche, R. Experimental and theoretical study of structural properties and phase transitions in YAsO4 and YCrO4. *Phys. Rev. B: Condens. Matter Mater. Phys.* **2011**, *83*, 134109.
(19) Konno, H.; Aoki, Y.; Klencsár, Z.; Vértes, A.; Wakeshima, M.; Tezuka, K.; Hinatsu, Y. Structure of EuCrO4 and Its Electronic and Magnetic Properties. *Bull. Chem. Soc. Jpn.* **2001**, *74*, 2335−2341.
(20) Chen, Q.; Sari, D.; Rutt, A.; Kim, J.; Ceder, G.; Persson, K. A. Zircon Structure as a Prototype Host for Fast Monovalent and Divalent Ionic Conduction. *Chem. Mater.* **2023**, *35*, 6313−6322.
(21) Li, L.-P.; Li, G.-S.; Xue, Y.-F.; Inomata, H. Structure, Luminescence, and Transport Properties of EuVO4. *J. Electrochem. Soc.* **2001**, *148*, J45.
(22) Esaka, T. Cation conduction in zircon-type solid solution based on YPO4. *Solid State Ionics* **1989**, *34*, 287−291.
(23) Rutt, A.; Sari, D.; Chen, Q.; Kim, J.; Ceder, G.; Persson, K. A. Novel Structural Motif To Promote Mg-Ion Mobility: Investigating ABO4 Zircons as Magnesium Intercalation Cathodes. *ACS Appl. Mater. Interfaces* **2023**, *15*, 34983−34991.
(24) Finch, R. J. Structure and Chemistry of Zircon and Zircon-Group Minerals. *Rev. Mineral. Geochem.* **2003**, *53*, 1−25.
(25) Shen, J. X.; Horton, M.; Persson, K. A. A charge-density-based general cation insertion algorithm for generating new Li-ion cathode materials. *npj Comput. Mater.* **2020**, *6*, 161.
(26) Shen, J.-X.; Li, H. H.; Rutt, A.; Horton, M. K.; Persson, K. A. Topological graph-based analysis of solid-state ion migration. *npj Comput. Mater.* **2023**, *9*, 99.
(27) Rutt, A.; Shen, J.-X.; Horton, M.; Kim, J.; Lin, J.; Persson, K. A. Expanding the Material Search Space for Multivalent Cathodes. *ACS Appl. Mater. Interfaces* **2022**, *14*, 44367−44376.
(28) Gunter, D.; Cholia, S.; Jain, A.; Kocher, M.; Persson, K.; Ramakrishnan, L.; Ong, S. P.; Ceder, G. Community Accessible Datastore of High-Throughput Calculations: Experiences from the Materials Project. In *2012 SC Companion: High Performance Computing, Networking Storage and Analysis*; IEEE: Salt Lake City, UT, USA, 2012; pp 1244−1251.
(29) Ong, S. P.; Richards, W. D.; Jain, A.; Hautier, G.; Kocher, M.; Cholia, S.; Gunter, D.; Chevrier, V. L.; Persson, K. A.; Ceder, G. Python Materials Genomics (pymatgen): A robust, open-source python library for materials analysis. *Comput. Mater. Sci.* **2013**, *68*, 314−319.
(30) Aykol, M.; Dwaraknath, S. S.; Sun, W.; Persson, K. A. Thermodynamic limit for synthesis of metastable inorganic materials. *Sci. Adv.* **2018**, *4*, No. eaaq0148.
(31) Sun, W.; Dacek, S. T.; Ong, S. P.; Hautier, G.; Jain, A.; Richards, W. D.; Gamst, A. C.; Persson, K. A.; Ceder, G. The thermodynamic scale of inorganic crystalline metastability. *Sci. Adv.* **2016**, *2*, No. e1600225.
(32) Rong, Z.; Kitchaev, D.; Canepa, P.; Huang, W.; Ceder, G. An efficient algorithm for finding the minimum energy path for cation migration in ionic materials. *J. Chem. Phys.* **2016**, *145*, 074112.
(33) Perdew, J. P.; Burke, K.; Ernzerhof, M. Generalized Gradient Approximation Made Simple. *Phys. Rev. Lett.* **1996**, *77*, 3865−3868.
(34) Blöchl, P. E. Projector augmented-wave method. *Phys. Rev. B: Condens. Matter Mater. Phys.* **1994**, *50*, 17953−17979.
(35) Kresse, G.; Furthmüller, J. Efficient iterative schemes for ab initio total-energy calculations using a plane-wave basis set. *Phys. Rev. B: Condens. Matter Mater. Phys.* **1996**, *54*, 11169−11186.
(36) Mathew, K.; Montoya, J. H.; Faghaninia, A.; Dwarakanath, S.; Aykol, M.; Tang, H.; Chu, I. h.; Smidt, T.; Bocklund, B.; Horton, M.; et al. Atomate: A high-level interface to generate, execute, and analyze computational materials science workflows. *Comput. Mater. Sci.* **2017**, *139*, 140−152.
(37) Henkelman, G.; Jónsson, H. Improved tangent estimate in the nudged elastic band method for finding minimum energy paths and saddle points. *J. Chem. Phys.* **2000**, *113*, 9978−9985.
(38) Dathar, G. K. P.; Sheppard, D.; Stevenson, K. J.; Henkelman, G. Calculations of Li-Ion Diffusion in Olivine Phosphates. *Chem. Mater.* **2011**, *23*, 4032−4037.
(39) Ong, S. P.; Chevrier, V. L.; Hautier, G.; Jain, A.; Moore, C.; Kim, S.; Ma, X.; Ceder, G. Voltage, stability and diffusion barrier differences between sodium-ion and lithium-ion intercalation materials. *Energy Environ. Sci.* **2011**, *4*, 3680.
(40) Arroyo-de Dompablo, M. E.; Ponrouch, A.; Johansson, P.; Palacín, M. R. Achievements, Challenges, and Prospects of Calcium Batteries. *Chem. Rev.* **2020**, *120*, 6331−6357.
(41) Torres, A.; Casals, J. L.; Arroyo-de Dompablo, M. E. Enlisting Potential Cathode Materials for Rechargeable Ca Batteries. *Chem. Mater.* **2021**, *33*, 2488−2497.
(42) Wang, A.; Kingsbury, R.; McDermott, M.; Horton, M.; Jain, A.; Ong, S. P.; Dwaraknath, S.; Persson, K. A. A framework for quantifying uncertainty in DFT energy corrections. *Sci. Rep.* **2021**, *11*, 15496.
(43) Hautier, G.; Ong, S. P.; Jain, A.; Moore, C. J.; Ceder, G. Accuracy of density functional theory in predicting formation energies of ternary oxides from binary oxides and its implication on phase stability. *Phys. Rev. B: Condens. Matter Mater. Phys.* **2012**, *85*, 155208.
(44) Ong, S. P.; Wang, L.; Kang, B.; Ceder, G. LiFePO2 Phase Diagram from First Principles Calculations. *Chem. Mater.* **2008**, *20*, 1798−1807.
(45) Jain, A.; Ong, S. P.; Hautier, G.; Chen, W.; Richards, W. D.; Dacek, S.; Cholia, S.; Gunter, D.; Skinner, D.; Ceder, G.; Persson, K. A. Commentary: The Materials Project: A materials genome approach to accelerating materials innovation. *APL Mater.* **2013**, *1*, 011002.
(46) Urban, A.; Seo, D.-H.; Ceder, G. Computational understanding of Li-ion batteries. *npj Comput. Mater.* **2016**, *2*, 16002.
(47) Hannah, D. C.; Sai Gautam, G.; Canepa, P.; Ceder, G. On the Balance of Intercalation and Conversion Reactions in Battery Cathodes. *Adv. Energy Mater.* **2018**, *8*, 1800379.
(48) Arthur, T. S.; Zhang, R.; Ling, C.; Glans, P.-A.; Fan, X.; Guo, J.; Mizuno, F. Understanding the Electrochemical Mechanism of K-αMnO2 for Magnesium Battery Cathodes. *ACS Appl. Mater. Interfaces* **2014**, *6*, 7004−7008.

https://doi.org/10.1021/acs.chemmater.4c00062
Chem. Mater. XXXX, XXX, XXX−XXX

(49) O'Keeffe, M. A proposed rigorous definition of coordination number. *Acta Crystallogr., Sect. A* **1979**, *35*, 772−775.
(50) Pan, H.; Ganose, A. M.; Horton, M.; Aykol, M.; Persson, K. A.; Zimmermann, N. E.; Jain, A. Benchmarking Coordination Number Prediction Algorithms on Inorganic Crystal Structures. *Inorg. Chem.* **2021**, *60*, 1590−1603.
(51) Aurbach, D.; Lu, Z.; Schechter, A.; Gofer, Y.; Gizbar, H.; Turgeman, R.; Cohen, Y.; Moshkovich, M.; Levi, E. Prototype systems for rechargeable magnesium batteries. *Nature* **2000**, *407*, 724−727.
(52) Gershinsky, G.; Yoo, H. D.; Gofer, Y.; Aurbach, D. Electrochemical and Spectroscopic Analysis of Mg2+ Intercalation into Thin Film Electrodes of Layered Oxides: V2O5 and MoO3. *Langmuir* **2013**, *29*, 10964−10972.
(53) Sotoudeh, M.; Groß, A. Stability of Magnesium Binary and Ternary Compounds for Batteries Determined from First Principles. *J. Phys. Chem. Lett.* **2022**, *13*, 10092−10100.
(54) Ramos, E. P.; Zhang, Z.; Assoud, A.; Kaup, K.; Lalère, F.; Nazar, L. F. Correlating Ion Mobility and Single Crystal Structure in Sodium-Ion Chalcogenide-Based Solid State Fast Ion Conductors: Na11Sn2PnS12 (Pn = Sb, P). *Chem. Mater.* **2018**, *30*, 7413−7417.
(55) Krauskopf, T.; Culver, S. P.; Zeier, W. G. Bottleneck of Diffusion and Inductive Effects in Li10Ge(1−x)SnxP2S12. *Chem. Mater.* **2018**, *30*, 1791−1798.
(56) He, X.; Zhu, Y.; Epstein, A.; Mo, Y. Statistical variances of diffusional properties from ab initio molecular dynamics simulations. *npj Comput. Mater.* **2018**, *4*, 18.
(57) Deng, Z.; Zhu, Z.; Chu, I.-H.; Ong, S. P. Data-Driven First-Principles Methods for the Study and Design of Alkali Superionic Conductors. *Chem. Mater.* **2017**, *29*, 281−288.
(58) Malik, R.; Burch, D.; Bazant, M.; Ceder, G. Particle Size Dependence of the Ionic Diffusivity. *Nano Lett.* **2010**, *10*, 4123−4127.
(59) Zhang, R.; Ling, C. Unveil the Chemistry of Olivine FePO4 as Magnesium Battery Cathode. *ACS Appl. Mater. Interfaces* **2016**, *8*, 18018−18026.
(60) Waroquiers, D.; Gonze, X.; Rignanese, G.-M.; Welker-Nieuwoudt, C.; Rosowski, F.; Göbel, M.; Schenk, S.; Degelmann, P.; André, R.; Glaum, R.; Hautier, G. Statistical Analysis of Coordination Environments in Oxides. *Chem. Mater.* **2017**, *29*, 8346−8360.
(61) Gangadharachar, R.; Chandrappa, G. T. Solution Combustion Synthesis of YVO4 Nanopowder Using V2O5.nH2O Gel: Photo-degradation Studies. *Trans. Indian Ceram. Soc.* **2021**, *80*, 47−54.
(62) Nagabhushana, G.; Tavakoli, A.; Navrotsky, A. Energetics of bismuth vanadate. *J. Solid State Chem.* **2015**, *225*, 187−192.

https://doi.org/10.1021/acs.chemmater.4c00062
Chem. Mater. XXXX, XXX, XXX−XXX